

PAPER

Incorporation of fragmentation into a volume average solidification model

To cite this article: Y Zheng *et al* 2018 *Modelling Simul. Mater. Sci. Eng.* **26** 015004

View the [article online](#) for updates and enhancements.

Incorporation of fragmentation into a volume average solidification model

Y Zheng¹, M Wu^{1,2} , A Kharicha^{1,2} and A Ludwig¹

¹ Chair of Modelling and Simulation of Metallurgical Processes, Montanuniversitaet Leoben, Austria

² Christian Doppler Laboratory for Advanced Simulation of Solidification and Melting, Montanuniversitaet Leoben, Austria

E-mail: menghuai.wu@unileoben.ac.at

Received 5 May 2017, revised 1 August 2017

Accepted for publication 17 August 2017

Published 5 December 2017



CrossMark

Abstract

In this study, a volume average solidification model was extended to consider fragmentation as a source of equiaxed crystals during mixed columnar-equiaxed solidification. The formulation suggested for fragmentation is based on two hypotheses: the solute-driven remelting is the dominant mechanism; and the transport of solute-enriched melt through an interdendritic flow in the columnar growth direction is favorable for solute-driven remelting and is the necessary condition for fragment transportation. Furthermore, a test case with Sn-10 wt% Pb melt solidifying vertically downward in a 2D domain ($50 \times 60 \text{ mm}^2$) was calculated to demonstrate the model's features. Solidification started from the top boundary, and a columnar structure developed initially with its tip growing downward. Furthermore, thermo-solutal convection led to fragmentation in the mushy zone near the columnar tip front. The fragments transported out of the columnar region continued to grow and sink, and finally settled down and piled up in the bottom domain. The growing columnar structure from the top and pile-up of equiaxed crystals from the bottom finally led to a mixed columnar-equiaxed structure, in turn leading to a columnar-to-equiaxed transition (CET). A special macrosegregation pattern was also predicted, in which negative segregation occurred in both columnar and equiaxed regions and a relatively strong positive segregation occurred in the middle domain near the CET line. A parameter study was performed to verify the model capability, and the uncertainty of the model assumption and parameter was discussed.

Keywords: solidification, fragmentation, volume average model, macrosegregation, columnar-to-equiaxed transition

(Some figures may appear in colour only in the online journal)

1. Introduction

Volume-average based multiphase solidification models were recently developed and applied to calculate the formation of as-cast structure and macrosegregation for industry castings [1–4]. The following solidification features are mostly considered: the progress of columnar tip front and evolution of columnar dendrite structure, nucleation and growth of equiaxed crystals, melt flow and equiaxed crystal sedimentation, solute partitioning at the solid/liquid interface, transport of the solute species and formation of macrosegregation, interaction or competition between growing columnar and equiaxed phases, and occurrence of columnar-to-equiaxed transition (CET). However, for most such models, the origin of the equiaxed crystals was simply treated as a continuous undercooling-dependent heterogeneous nucleation event [5, 6] or a simultaneous nucleation event at a certain undercooling [4]. The number of equiaxed crystals created through fragmentation was ignored or simplified, although many laboratory experiments [7–9] and industry practices [10] have confirmed its importance.

Fragmentation has been understood through two main mechanisms: the mechanism of the mechanical fracture of the crystal dendrites, and mechanism of dendrite remelting. As early as the 1960s, Chalmers and Williamson [11] observed the formation of ice crystals in the flowing and undercooled waters and determined that mechanical rupture (fracture) was responsible for their origin. By submerging bulk ice in flowing and slightly-undercooled ($-0.2\text{ }^{\circ}\text{C}$) water, new ice crystals in the shape of small discs were observed to grow immediately from the ice substrate. As the connection of the ice discs with the substrate of the bulk ice was very weak, they were washed away from it by the flow. Based on these experimental observation, Chalmers and Williamson [11] anticipated that this type of ‘crystal multiplication’ mechanism through mechanical rupturing would occur in metal castings by the agitation of the melt during freezing. However, a later experiment conducted by Garabedian *et al* [12] with the same type of water showed that it was very difficult to produce the ‘crystal breeding,’ that is, crystal multiplication by pure fluid sheering. A growing ice crystal was rotated in the undercooled water to create a shear force on the ice dendrites. By sheering the water with a velocity as high as 1.5 m s^{-1} , the ice crystals could not be broken. In the late 1990s, Pilling and Hellawell [13] performed a theoretical calculation for the metal alloy, and determined that the maximum stress of a dendrite arm at its weakest point (connection with the primary dendrite) under the shear flow would only reach approximately 1% of the estimated yield strength of the material at its melting point. They concluded that the interdendritic flow does not contribute directly to the crystal multiplication because of dendrite fracturing. This conclusion was confirmed by Mullis *et al* [14] with a recent calculation, for which they stated that ‘under most conditions, the likelihood of dendrites experiencing mechanical damage due to flow of the parent melt is remote.’ The fragmentation caused by remelting the dendrite stem was first proposed by Jackson *et al* through an $\text{NH}_4\text{Cl-H}_2\text{O}$ solidification experiment [15]. Forced flow during solidification was introduced by stirring the melt by using a motor-driven propeller. It was suggested that fragmentation resulted from solute rejection during dendrite growth, producing favorable conditions for the remelting of a side branch at its base and leading to subsequent ‘pinch off.’ The heat and solute generated by the growth of side branches increases the local temperature and solute concentration; this is experienced by the base of the side branches leading to the occurrence of ‘constitutional’ remelting. Stirring was performed to create or enhance the interdendritic flow necessary for transporting the fragments out of the mushy zone. This remelting-induced fragmentation theory was later supported by many follow-up experiments, for example, by using similar $\text{NH}_4\text{Cl-H}_2\text{O}$

solutions [16–18], other model alloys (succinonitrile (SCN)-acetone) [19], and even metal alloys [9, 20–22]. The method of synchrotron x-ray radiography provided an opportunity to perform *in situ* observation of the fragmentation process of metal alloys during solidification at the elevated temperature. Solute-driven remelting seems to be the dominant mechanism for fragmentation, although many authors still believe that mechanical fractures cannot be ignored [18]. Regardless of the mechanism being operated, the importance of the flow is confirmed by almost all the above-mentioned studies: (1) the flow influences the transport of the fragments and (2) promotes or retards the remelting of the dendrite stems through solute transportation.

According to Hellowell *et al* [7], five steps are necessarily considered for evaluating the fragmentation event and its consequence on the as-cast structure formation: (1) dendrite arms are first fragmented/detached from the columnar dendrites; (2) fragments are transported through the mushy zone by interdendritic flow; (3) fragments during transport through the mushy zone survive the superheat; (4) fragments continue to grow in the bulk melt; and (5) equiaxed grains grow from those fragment sediments and interact with the columnar structure, and they might be entrapped into and block the columnar structure, leading to CET. In reality, some multiphase volume average models [2, 3] have already considered steps (2)–(5). Moreover, the treatment of step (1) can be decided by answering the following questions. What is the production rate of the fragments, and what is its correlation with the thermal or solutal fields, interdendritic flow, and dendrite morphology (fraction of solid, primary, and secondary spaces)? What is the (average) size of the fragments? This information is needed by the volume average solidification model for defining the source term for the transport equation of the number density of equiaxed crystals, for defining mass and energy transfers between the columnar structure phase and the newly formed fragments, as part of the equiaxed phase. In the multiphase transport system, ‘fragmentation’ implies that a certain number of detached dendrite arms from the columnar structure will be converted into equiaxed structure, and correspondingly a certain amount of mass and energy will be transferred into the equiaxed phase.

Experiments were also conducted for performing fragment count. For example, Paradies *et al* [19] performed a solidification experiment under forced flow condition based on a model alloy, that is, SCN-acetone. They attempted to count the number of detached fragments at the front of the mushy zone. Fragments that cannot be transported out of the mushy zone (fully remelted or locked into the dendrite network) were ignored. Based on this fragment count, they estimated the fragment production rate. The dimension of the field of view (in which the fragments were counted) seems large enough for performing statistical analysis. The original purpose of this study was to establish a correlation between the fragmentation rate and the experiment-controlling parameters, that is, the cooling rate, forced flow rate, and initial alloy composition; however, this attempt was unsuccessful. Although the velocity adjacent to the mushy zone appeared to correlate well with the fragmentation rate from the experiment of one alloy (SCN-1.3 wt% acetone), this correlation contradicted with the experiment of another alloy (SCN-6.1 wt% acetone). The size of fragments was not measured. Montgomery *et al* [18] performed another fragment count experiment based on the solidification of $\text{NH}_4\text{Cl-H}_2\text{O}$ solutions under natural convection conditions. The fragments were counted ahead of the mushy zone, and both the number and volume fraction of fragments were measured (from which average size of fragments can be estimated). Again, this study could only provide some information for understanding the production, development, and transport of crystal fragments but failed to establish a quantitative correlation of the fragmentation rate with the flow, thermal, and alloy composition parameters. By using the synchrotron x-ray radiography, Liotti *et al* attempted

to count the fragmentation rate during solidification of metal alloys (Al-15 wt%Cu) [22]. A pulsed electromagnetic field was introduced to create a pulse flow in the interdendritic region, and the following valuable information was obtained. The introduced pulse flow enhances the fragmentation through the remelting mechanism; fragmentation is not a phenomenon confined to the front mushy region but is spread throughout a wide range of the mushy zone with high solid fraction. Unfortunately, owing to the limited dimensions of the specimen (200 μm) the transport of the fragments by flow through the mushy zone into the bulk melt region cannot be studied using this method. Fragments created in the deep mushy zone are not necessarily counted as active nuclei of equiaxed crystals because they cannot be transported into the bulk melt [7].

Lesoult [10] reported a very valuable study for steel based on a hypothesis that stirring of molten steel before the solidification of the front would result in seeding of the liquid with dendritic fragments. Presumably, those fragments were eroded from the columnar tip front. He determined that the fragment flux quantified by the number of crystals eroded per unit time and area of the columnar solidification front ($\text{cm}^{-2} \text{s}^{-1}$) correlated with the tangential velocity of the liquid along the solidification front. For example, under intensity stirring (tangential liquid velocity up to 1 m s^{-1}), the fragment flux reached as high as $10\text{--}100 \text{ cm}^{-2} \text{ s}^{-1}$. In addition, under natural convection condition (tangential liquid velocity of 1 cm s^{-1}), the fragment flux would be reduced to approximately $1 \text{ cm}^{-2} \text{ s}^{-1}$. This concept was later implemented into a multiphase solidification model to calculate the fragmentation phenomenon during a mixed columnar-equiaxed solidification of steel [23]. As the size and shape of the newly eroded fragments were not available, they were assumed to be spheres with diameter of $1 \mu\text{m}$. This numerical treatment seems reasonable for a solidification model but the experimentally determined relationship of the fragment flux with the tangential liquid velocity does not directly correlate with the solute-driven remelting mechanism of the fragmentation. According to the classical solidification theory [24], it is the flow in the growth direction of the primary columnar dendrites, rather than the tangential liquid velocity, that may promote the remelting of the dendrites.

Based on the Flemings' theory for local remelting of the mushy zone [24], Campanella *et al* derived an onset criterion for remelting-induced fragmentation [25]. That is, fragmentation occurs when the component of the fluid flow velocity in the thermal gradient direction, presumably coinciding with the growth direction of the primary columnar dendrites, becomes larger than the speed of the isotherms at a depth of $6\text{--}8 \lambda_2$ (secondary dendrite arm space) in the mushy zone. This implies that the flow transports a solute-enriched melt from the deep interdendritic region into the front region of the mushy zone, reducing the melting point, and hence promoting the remelting of dendrite arms in that region. Additionally, the flow in the columnar growth direction is necessary for transporting fragments out of the mushy zone. The shortcoming of this onset criterion is that no quantitative information is provided about the production rate and size of the fragments.

Inspired by the work of Campanella *et al* [25], in this study, a local remelting-based formulation for the fragmentation is suggested and implemented in a three-phase mixed columnar-equiaxed solidification model [6, 26]. The test case was calculated to show the model features. A series of simulations were conducted to study the sensitivity of the modeling result to the numerical and modeling parameters.

2. The model

A three-phase mixed columnar-equiaxed solidification model has been described previously [6, 26]. As the columnar dendrite structure and the equiaxed grains (crystals) are treated as two separate solid phases, their evolutions through solidification are calculated explicitly. In addition, their amounts are quantified by their volume fractions, f_c and f_e , respectively. The columnar phase is stationary ($\bar{u}_c \equiv 0$), and the morphological parameters, such as the primary and secondary arm spaces, λ_1 and λ_2 , are predefined (experimental data from literature). The equiaxed phase motion \bar{u}_e is calculated by solving the corresponding momentum conservation equation. The transport of the number density of the equiaxed crystals n_{eq} must be calculated as

$$\frac{\partial}{\partial t} n_{eq} + \nabla \cdot (\bar{u}_e n_{eq}) = N, \quad (1)$$

by considering a source term N , which should include three parts [27]: the heterogeneous nucleation N_{nucl} , fragmentation N_{frag} , and death by dissolution (remelting) N_{remelt} . As soon as n_{eq} is determined, the average diameter of the equiaxed grains (d_e) can be calculated. For the globular equiaxed crystal, $d_e = \sqrt[3]{6f_e/\pi n_{eq}}$. If the crystal is dendritic, a concept of the dendritic crystal envelop is employed; the fraction solid inside the dendritic crystal envelop, that is, f_{si} must be calculated [28, 29] or presumed [30], and then the diameter of the equiaxed grain envelope can be estimated by $d_e^{env} = d_e/\sqrt[3]{f_{si}}$. In this study, a constant f_{si} value of 0.5 is used.

2.1. Remelting-induced fragmentation

It is known that the transport of the solute-enriched melt through the interdendritic flow in the columnar-growth direction would lead to remelting [24, 25]. Under normal diffusion-governed solidification/remelting condition, the driving force for the remelting is the constitutional supersaturation ($c_\ell - c_\ell^*$), where c_ℓ is the volume-averaged concentration of interdendritic melt; c_ℓ^* is the thermodynamic equilibrium concentration of the melt at the liquid–solid interface. If the curvature effect is considered, $c_\ell^* = \frac{T - T_f}{m} - \frac{\Gamma}{m} \left(\frac{1}{r_1} - \frac{1}{r_2} \right)$. A positive value of ($c_\ell - c_\ell^*$) results in remelting, or a process leading to an increase of c_ℓ promotes remelting. The influence of the interdendritic flow on c_ℓ^* is very limited. Furthermore, the curvature of the dendrite stem is independent from the flow, whose influence on the local temperature T is ignorable compared with its influence on solute concentration (because of large Lewis number of metal alloys). The interdendritic melt usually has a concentration gradient (∇c_ℓ) contradictory to the columnar growth direction of alloys with the solute partition coefficient (k) less than one (figure 1). An interdendritic flow in the columnar growth direction indicates $-(\bar{u}_\ell - \bar{u}_c) \cdot \nabla c_\ell > 0$. Here, \bar{u}_ℓ and \bar{u}_c denote the liquid velocity and the columnar phase velocity, respectively. Therefore, the flow leads to a local increase in c_ℓ , promoting the remelting. Actually, the rate of remelting should be proportional to the value of $-(\bar{u}_\ell - \bar{u}_c) \cdot \nabla c_\ell$. Even if the local capillary effect, that is, the coarsening or ripening phenomenon is ignored, fragments can be produced by the ‘homogenous’ remelting. Based on the large number of experimental facts on the remelting-induced fragmentation [15–22] and the above-mentioned theoretical analysis, we assume that the rate of fragmentation is proportional to the value of $-(\bar{u}_\ell - \bar{u}_c) \cdot \nabla c_\ell$ by suggesting the following formulation for the fragmentation-induced mass transfer rate from the columnar to equiaxed phase:

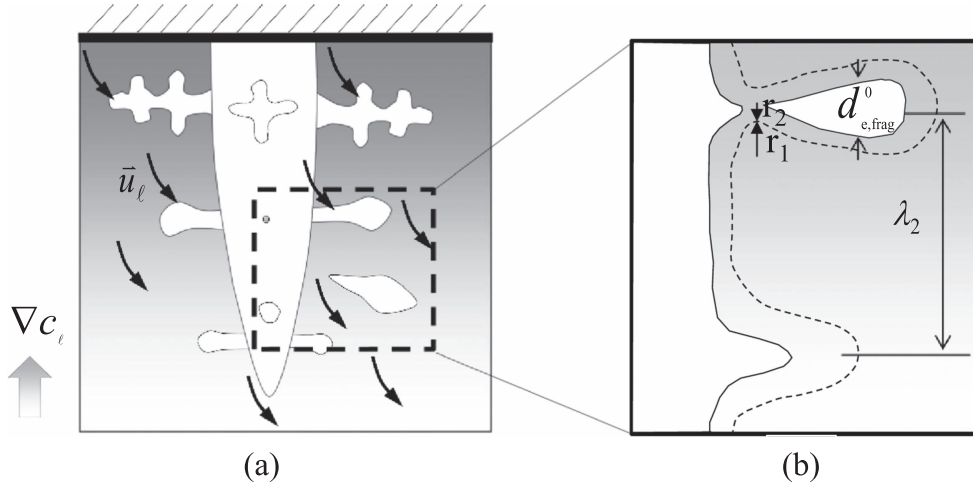


Figure 1. Schematic description of remelting-induced fragmentation: (a) transport of solute-enriched interdendritic melt through the flow, and (b) formation of a fragment by remelting of the side arm.

$$M_{ce} = -\gamma \cdot (\bar{u}_\ell - \bar{u}_c) \cdot \nabla c_\ell \cdot \rho_e. \quad (2)$$

Note that fragmentation occurs only with remelting, that is, when $M_{ce} > 0.0$. For solidification (calculated M_{ce} has a negative value), we set $M_{ce} = 0.0$ to prevent the occurrence of fragmentation. The mass integral of all fragments as produced per time ($\text{kg m}^{-3} \text{s}^{-1}$) is proportional to the increase rate of constitutional supersaturation caused by the interdendritic flow. Here, a fragmentation coefficient γ was assigned to bridge the unknown correlation between M_{ce} and the increase rate of constitutional supersaturation. In other words, all other unknown contributing factors, such as the curvature effect of the dendrites, latent heat-induced thermal fluctuation, and diffusion in the interdendritic melt, for the remelting-induced fragmentation are included in the single coefficient γ . γ has a positive value for the alloy with the solute partition coefficient $k < 1$, a negative value for the alloy with $k > 1$. The coefficient must be determined experimentally, or estimated reversely from some available experimental information. Section 4.2 presents the parameter study on γ .

As shown in figure 1, we assume that the fragment is globular (spherical). The diameter of the fragment is proportional to the secondary dendrite arm spacing and the volume fraction of the columnar phase:

$$d_{e,frag}^0 = \lambda_2 f_c. \quad (3)$$

Here, f_c indicates the columnar phase volume fraction. Hence, the rate of the fragment production can be calculated as follows:

$$N_{frag} = \frac{M_{ce}}{\rho_e \cdot \frac{\pi}{6} (d_{e,frag}^0)^3}. \quad (4)$$

Correspondingly, the fragmentation-induced momentum transfer (\bar{U}_{ce}^p), energy transfer (Q_{ce}^p), and species transfer (C_{ce}^p) from the columnar to equiaxed phases are defined as follows:

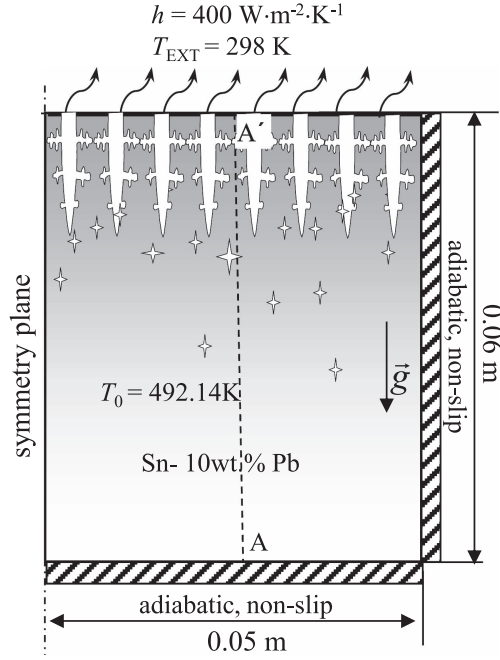


Figure 2. Configuration of the test case.

$$\vec{U}_{ce}^p = \vec{u}_c \cdot M_{ce}, \quad (5)$$

$$Q_{ce}^p = h_c \cdot M_{ce}, \quad (6)$$

$$C_{ce}^p = c_c \cdot M_{ce}, \quad (7)$$

where \vec{u}_c , h_c , and c_c are respectively the moving velocity, enthalpy, and concentration of the columnar phase. Several auxiliary quantities, such as macrosegregation index $c^{\text{index}} = (c_{\text{mix}} - c_0) \times 100/c_0$, mixture concentration $c_{\text{mix}} = (c_\ell \rho_\ell f_\ell + c_c \rho_c f_c + c_e \rho_e f_e) / (\rho_\ell f_\ell + \rho_c f_c + \rho_e f_e)$, and global macrosegregation intensity $\text{GMI} = \left(\iiint_{V_{\text{domain}}} |c^{\text{index}}| dV \right) / V_{\text{domain}}$, are used to analyze the macrosegregation [31, 32].

2.2. Test-case configuration and numerical implementation

Figure 2 shows the configuration of a 2D test case. The geometry is obtained from the benchmark defined by Bellet *et al* [33]; however, in this study, only half of the benchmark is calculated by setting a symmetry plane at the left boundary. Heat is only extracted through the top wall with a heat transfer coefficient $h = 400 \text{ W m}^{-2} \text{ K}^{-1}$, while other walls are set as adiabatic boundaries. Moreover, an alloy of Sn-10 wt%Pb is considered. The solute element Pb is heavier than the solvent Sn, and the solidified equiaxed crystal is assumed to always be heavier than the melt. As a closed domain is calculated and no volume shrinkage is considered, the Boussinesq approximation is conducted for the thermo-solutal convection and crystal sedimentation. The test-case domain is initially filled with the stationary melt of its liquidus temperature, that is, no superheat and motion. Solidification with a columnar

Table 1. Material properties and other parameters.

	Symbol	Units		References
Nominal concentration	c_0	1	0.1	
Liquidus temperature	T_{liq}	K	492.14	[33]
Melting point of solvent at $c_0 = 0$	T_f	K	505	[33]
Eutectic composition	c_{eu}	1	0.381	[33]
Eutectic temperature	T_{eu}	K	456	[34]
Liquidus slope	m	K	-128.6	[33]
Equilibrium partition coefficient	k	1	0.0656	[33]
Reference density	ρ_{ref}	kg m^{-3}	7000	[33]
Specific heat	c_p^l, c_p^e, c_p^c	$\text{J kg}^{-1} \text{K}^{-1}$	260	[33]
Thermal conductivity	k_l, k_e, k_c	$\text{W m}^{-1} \text{K}^{-1}$	55.0	[33]
Latent heat	L	J kg^{-1}	6.1×10^4	[33]
Viscosity	μ_l	$\text{kg m}^{-1} \text{s}^{-1}$	1.0×10^{-3}	[33]
Liquid thermal expansion coefficient	β_T	K^{-1}	6.0×10^{-5}	[33]
Liquid solutal expansion coefficient	β_C	$\text{wt}\%^{-1}$	-5.3×10^{-3}	[33]
Primary dendritic arm spacing	λ_1	m	1.3×10^{-3}	[33]
Second dendritic arm spacing	λ_2	m	0.65×10^{-4}	[33]
Diffusion coefficient (liquid)	D_l	$\text{m}^2 \text{s}^{-1}$	4.5×10^{-9}	[35]
Diffusion coefficient (solid)	D_s, D_e	$\text{m}^2 \text{s}^{-1}$	1×10^{-12}	[35]
Initial temperature	T_0	K	492.14	[33]
Heat transfer coefficient	h	$\text{W m}^{-2} \text{K}^{-1}$	400	[33]
External temperature	T_{EXT}	K	298	[33]
Solid-liquid density difference	$\Delta\rho$	kg m^{-3}	304	[36]
Gibbs Thomson coefficient	Γ	m K	6.5×10^{-8}	[37]
Fragmentation coefficient	γ	1	0.1 (0.01, 1.0, 10.0)	

structure initiates from the top unidirectionally. Equiaxed crystals could be produced near the columnar region through fragmentation. Table 1 shows the thermodynamic data and thermal physical properties of alloy Sn-10 wt%Pb. In this study, we considered only one source term for equation (1): the origin of equiaxed crystals through fragmentation. The parts due to the heterogeneous nucleation N_{nuc1} and the death by dissolution (remelting) N_{remelt} were ignored.

The solidification model is developed within the framework of the CFD software ANSYS-Fluent version 14.5 [6, 26]. Calculations with maximum 30 iterations were set for each time step to decrease the residuals of continuity, momentum conservation, species transport, and user-defined scalar conservation equations to a value below the convergence criterion of 10^{-4} and the enthalpy conservation equations below that of 10^{-7} . Owing to the complexity of the multiphase coupling, the time step should be kept small (0.001–0.01 s) to satisfy the above-mentioned convergence criteria.

3. Simulation results

3.1. Solidification sequence

Figure 3 shows the solidification sequence of the test case. For this calculation, a constant fragmentation coefficient ($\gamma = 0.1$) was assumed. With the initiation of cooling, the growth of columnar trunks and thermo-solutal convection begin from the top. The velocity magnitude is calculated as 1.4 cm s^{-1} . At 5 s, as shown in figure 3(a.1), a columnar-liquid two-phase region

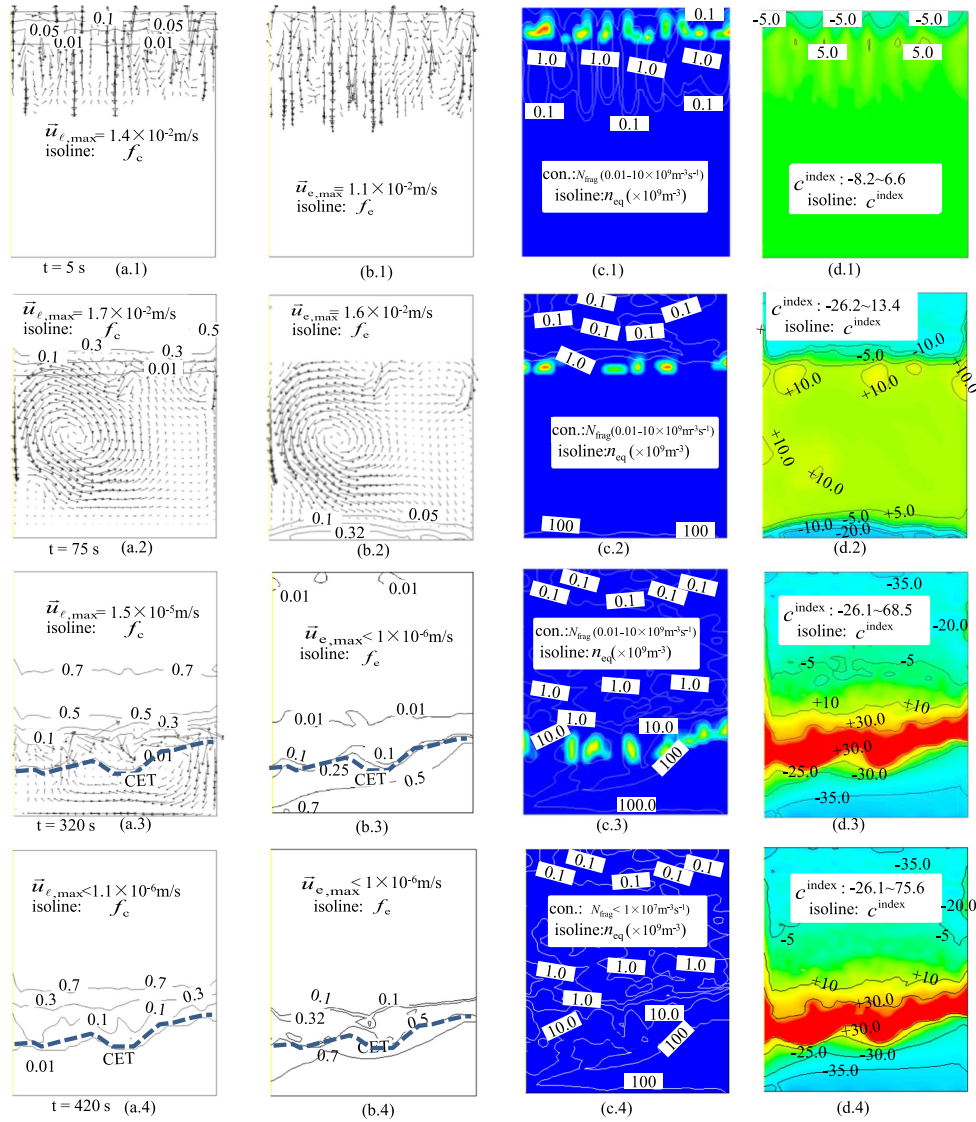


Figure 3. Solidification sequence of the test case: (a.x) show liquid velocity overlaid with f_c isoline; (b.x) show equiaxed velocity overlaid with f_c isoline; (c.x) show N_{frag} contour overlaid with n_{eq} isoline; and (d.x) show the contour of macrosegregation index (c_{index}). N_{frag} and c_{index} are represented in the color scales with blue for the minimum (or negative extreme), and red for the maximum (or positive extreme).

(mush) is developed. Some convection cells can penetrate into the mushy zone. Furthermore, fragmentation shown by the N_{frag} contour in figure 3(c.1) occurs in the mushy zone. The formation of the fragments seems nonuniform. Some ‘islands’ with local high fragmentation rate are found near the columnar tip front in the mushy zone; these fragments serve as nuclei for the equiaxed crystals. The number density N_{eq} achieves a magnitude of 10^9 m^{-3} . Moreover, the equiaxed crystals start growing and sinking; however, their motion is influenced by

the melt flowing through the drag force. Figure 3(b.1) shows the motion of the equiaxed crystals, with similar velocity magnitude to the melt flow.

At 75 s, the top mushy zone (columnar) extends to approximately 1/3 of the domain (figure 3(a.2)). A large vortex of melt flow and some small convection cells form in the bulk and near the columnar tip front regions, penetrating into the mushy zone (till $f_c \sim 0.3$). The melt flow has a significant impact on the velocity field of the equiaxed crystals (figure 3(b.2)). Both the melt flow and motion of equiaxed crystals have similar velocity magnitude: 1.7 and $1.6 \times 10^{-2} \text{ m s}^{-1}$. The equiaxed crystals finally settle at the bottom of the domain. As f_c reaches the packing limit, the equiaxed phase stops moving. This phenomenon is known as equiaxed settlement or sedimentation. A second mushy zone with packed equiaxed crystals develops from the bottom. The fragmentation continues near the columnar tip front (figure 3(c.2)), supplying equiaxed nuclei continuously. The maximum number density can reach a magnitude of 10^{11} m^{-3} .

At 320 s, the extension of the columnar mushy zone and the pile-up of the equiaxed mushy zone meet at approximately one-third height of the domain, figures 3(a.3)–(b.3). The growth of the columnar tip front is blocked by the equiaxed grain envelope mechanically, that is, CET occurs, as represented by the blue dash line. The melt flow is confined in the mushy zone, and its velocity magnitude is reduced to 10^{-5} m s^{-1} . This slow interdendritic flow still causes fragmentation in the columnar mushy zone above the CET line (figure 3(c.3)). The motion of equiaxed crystals is ignorable. These newly formed fragments cannot be transported out of the columnar mushy region but they will grow as equiaxed phase, competing with the growth of the columnar phase. In addition, a mixed columnar-equiaxed phase region is obtained above the CET line. Figures 3(a.4)–(c.4) show the solidification results at 420 s. The entire solidification sequence ends at 580 s, and the remaining melt in the mushy zone solidifies as a eutectic phase below temperature T_{eu} .

Figures 3(d.1)–(d.4) present the evolution of macrosegregation during solidification. At 5 s, the macrosegregation is weak, and a negative segregation occurs in the columnar mushy zone. A slightly positive segregation, following the pattern of the melt convection cells, is obtained before the columnar tip front. At 75 s, with the extension of the columnar mushy zone, the negative segregation (both the strength and area) increases. The positive segregation in the bulk melt region due to the mixing effect of the melt flow and crystals sedimentation becomes relatively homogenous. The equiaxed mushy zone near the bottom bears negative segregation. This process continues until the CET occurs at 320 s. The region of the middle positive segregation is gradually reduced to a relatively narrow region between the top negatively-segregated columnar mushy zone and the bottom negatively-segregated equiaxed mushy zone. The intensity of the positive segregation increases there. The solidification process ends at 580 s. The location of the final solidification is near the CET line. After the CET event, the global segregation distribution patterns remain.

3.2. Formation and transport of fragments

Figure 4 shows fragmentation-induced mass transfer rate (M_{ce}) from the columnar to equiaxed phases in the solidifying domain at 3 s. The number of fragments newly produced (N_{frag}) is proportional to M_{ce} . Fragments are mainly located in the mushy zone near the columnar tip front, which is indicated by isoline $f_c = 0.01$. According to the model (equation (2)), the interdendritic flow in the direction against the liquid concentration gradient direction leads to local increase of c_ℓ , promoting remelting and fragmentation. This can be witnessed from the detailed view (Zone 1) of the liquid velocity \vec{u}_ℓ (white) and liquid concentration gradient ∇c_ℓ

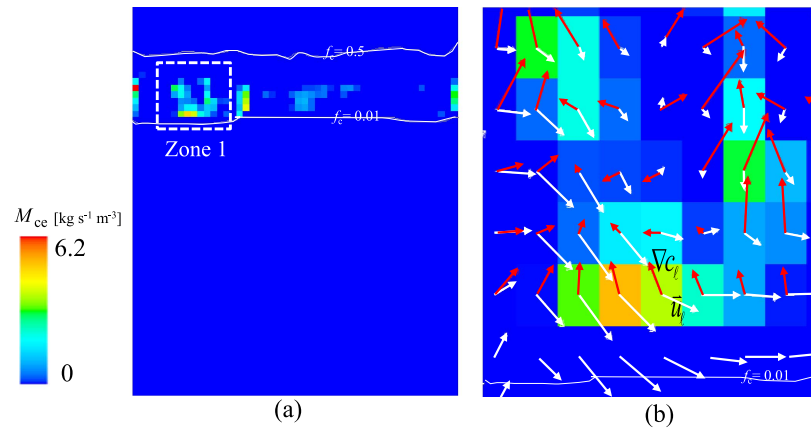


Figure 4. Fragmentation-induced columnar-to-equiaxed mass transfer at 3 s: (a) global view of M_{ce} contour and (b) zoom-in view of Zone 1 overlaid with liquid velocity \bar{u}_ℓ (white) and liquid concentration gradient ∇c_ℓ (red). Isolines of f_c are plotted in (a), indicating the position of columnar mushy zone.

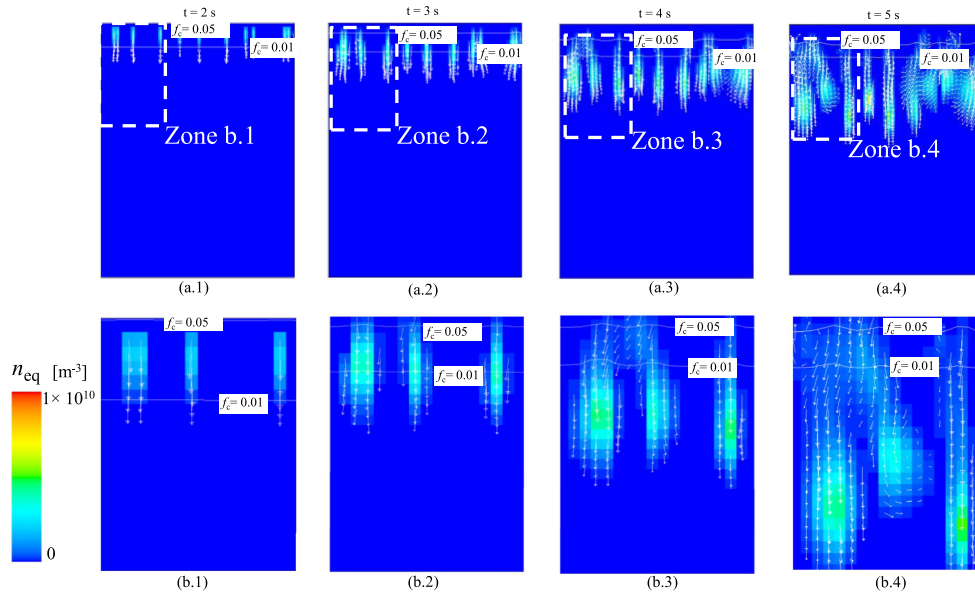


Figure 5. Evolution of equiaxed number density (n_{eq}) from 2 to 5 s: (a.x) show the global view of n_{eq} contour overlaid with liquid velocity \bar{u}_ℓ (white); (b.x) show the zoom-in view of Zone (b.x). Isolines of f_c are plotted in (a.x), indicating the position of columnar mushy zone.

(red) in figure 4(b). In the region where fragmentation-induced mass transfer occurs ($M_{ce} > 0.0$), the angle between the two vectors (\bar{u}_ℓ , ∇c_ℓ) is larger than 90° .

As soon as new fragments are created in the columnar mushy zone, they act as nuclei of equiaxed crystals. The equiaxed number density (n_{eq}) increases locally, and they can be transported with the velocity of \bar{u}_ℓ . Figure 5 shows the detailed analysis of the transport of n_{eq}

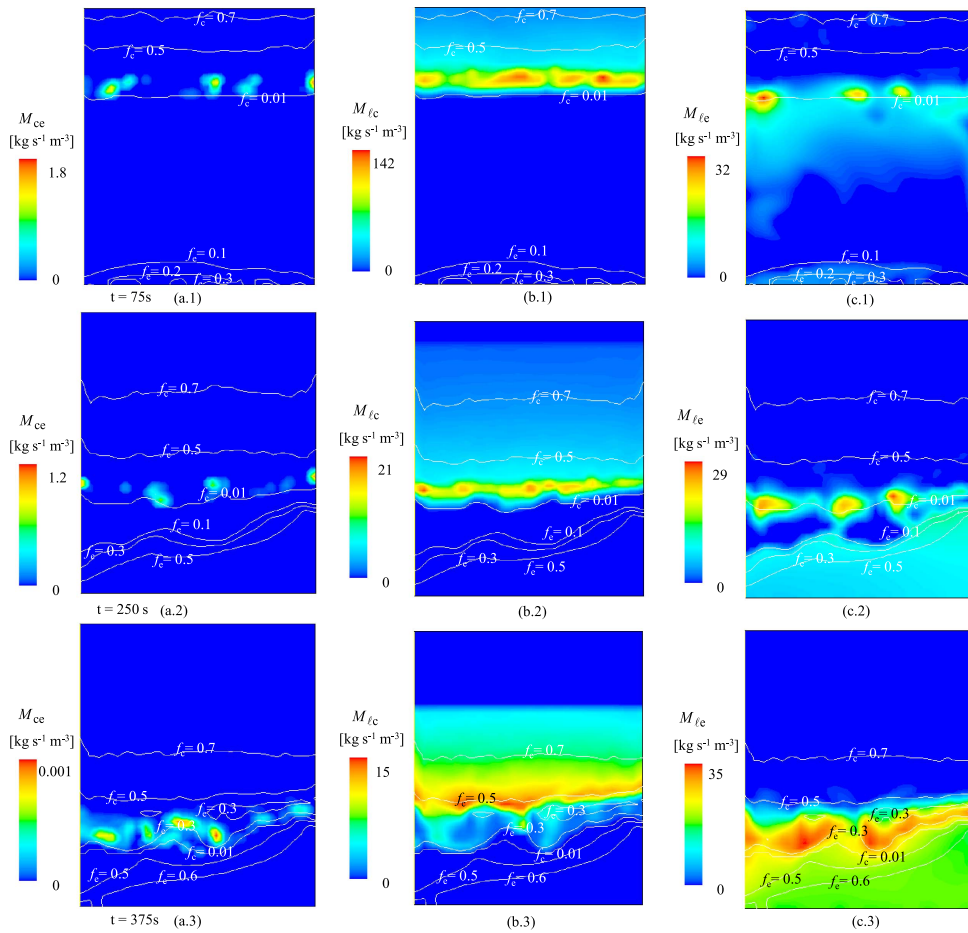


Figure 6. Balance of mass transfer among M_{ce} , M_{lc} , and M_{le} (75, 250 and 375 s). (a.x) contour of M_{ce} overlaid with f_e and f_c isolines; (b.x) contour of M_{lc} overlaid with f_e and f_c isolines; (c.x) contour of M_{le} overlaid with f_e and f_c isolines.

by \bar{u}_e . With the solidification, equiaxed crystals, that is, n_{eq} , are gradually transported out of the columnar mushy zone into the bulk region. In addition, new fragments, as new nuclei of equiaxed crystals, are continuously produced in the mushy zone. Generally, the equiaxed velocity is pointed downward because of the larger density of solid than that of liquid; however, the motion of the equiaxed phase (\bar{u}_e) in the bulk region is significantly influenced by the melt convection.

The balance between the fragmentation-induced mass transfer (M_{ce}) and solidification-induced mass transfer (M_{lc} , M_{le}) is analyzed in figure 6. At the early stage of solidification (75 s), solidification-induced mass transfer rate M_{lc} (maximum $142 \text{ Kg m}^{-3} \text{ s}^{-1}$) is much larger than fragmentation-induced mass transfer rate M_{ce} (maximum $1.8 \text{ Kg m}^{-3} \text{ s}^{-1}$). The solidification rate of the columnar phase overweighs the fragmentation-induced mass transfer rate. Furthermore, M_{le} (maximum $32.0 \text{ Kg m}^{-3} \text{ s}^{-1}$) is also much larger than M_{ce} . When the solidification proceeds to 250 s, M_{ce} is still at the magnitude of $1.2 \text{ Kg m}^{-3} \text{ s}^{-1}$, while the maximal values of M_{lc} and M_{le} are 40 and $71 \text{ Kg m}^{-3} \text{ s}^{-1}$. During the late stage of

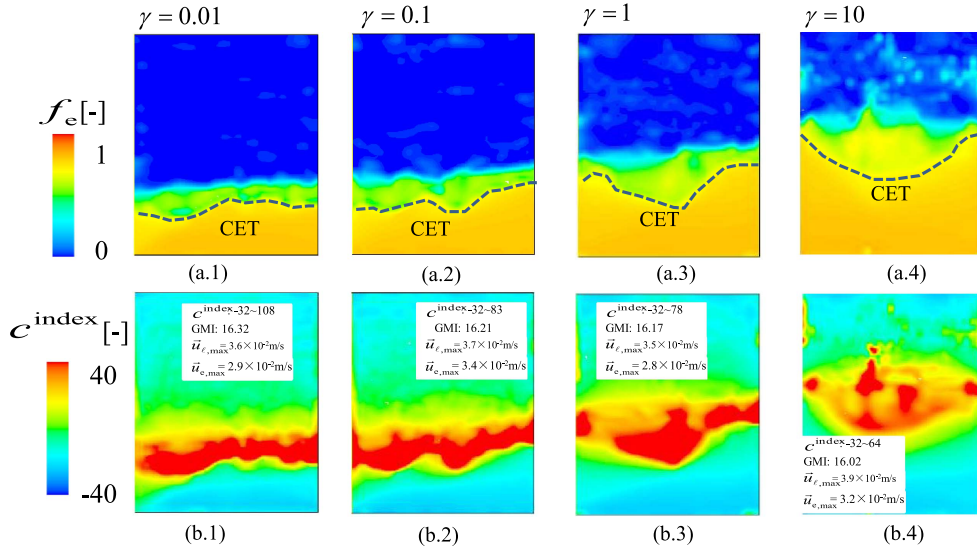


Figure 7. Influence of the chosen fragmentation coefficient γ on the as-cast structure and macrosegregation. (a.x) Distribution of equiaxed phase (the blue region above the CET line is dominated by the columnar phase). (b.x) Macrosegregation contour (c^{index}).

solidification (375 s), the columnar tip front is stopped by the pile of equiaxed crystals from the bottom, and CET occurs. At this moment, M_{ce} is insignificantly small (maximum $10^{-3} \text{ Kg m}^{-3} \text{ s}^{-1}$), thus fragmentation is almost terminated. However, the solidification of columnar and equiaxed phases continues. The main function of fragmentation, i.e. the effect of, M_{ce} is to supply the sites of equiaxed nuclei rather than to form equiaxed phase directly. The formation of equiaxed phase is mainly due to the growth of those equiaxed crystals during the subsequent solidification. We find that M_{ce} is always smaller than M_{lc} in the current test case. This correlation might apply for other alloys, but further study is needed to verify it. Note that fragmentation depends on the flow intensity, and in the current test case the thermal-solutal convection is weak (10^{-2} m s^{-1}).

4. Parameter study and discussion

4.1. Fragmentation coefficient γ and equiaxed sedimentation

It is well-accepted that the solute-driven remelting is the key mechanism for fragmentation; however, there is no theoretical model available for the fragmentation. In this study, a fragmentation coefficient γ was introduced (equation (2)) to bridge the unknown correlation between M_{ce} , N_{frag} , and the possible contributing factors for the remelting-induced fragmentation, such as the curvature effect of the dendrites, thermal fluctuation induced by the release of latent heat, and solute diffusion in the interdendritic melt. This coefficient should be determined experimentally. To determine the influence of γ on the solidification, four cases with different values of γ (0.01, 0.1, 1.0, and 10) were calculated. The end solidification results of these cases are compared in figure 7. For each case, a CET line separates two regions: the upper columnar region and the lower equiaxed region. Obviously, the equiaxed region increases with the influence of the chosen γ . Owing to equiaxed crystal sedimentation,

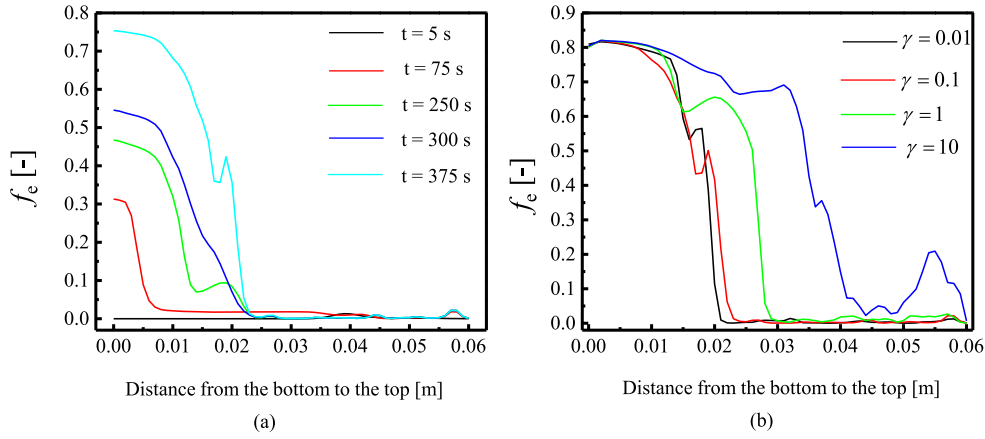


Figure 8. (a) Evolution of f_e along the vertical line A-A', as marked in figure 2 during solidification when $\gamma = 0.1$; (b) Influence of γ on f_e distribution along the vertical line A-A' at the end solidification.

a strong macrosegregation occurs for each case: negative segregations in both the upper columnar region and lower equiaxed region, and a positive segregation region sandwiched between the two just above the CET line. The macrosegregation range (c^{index}) and global macrosegregation index (GMI) are labeled in figures 7(b.1)–(b.4). The segregation intensity is correlated to the relative motion between the liquid and the settling equiaxed crystals [31, 32]; hence, the maximal liquid velocity $\vec{u}_{\ell, \text{max}}$ and equiaxed velocity $\vec{u}_{e, \text{max}}$ are also labeled. It is found that the influence of γ on $\vec{u}_{\ell, \text{max}}$ and $\vec{u}_{e, \text{max}}$ is not significant, and hence the influence of γ on segregation intensity is not significant. The major influence of γ is on the as-cast structure distribution.

Quantitative analyses were conducted for the equiaxed sedimentation along the vertical line A-A' marked in figure 2. Figure 8(a) presents the evolution of f_e . At 5 s, only a small amount of equiaxed phase is detected. In addition, at 75 s, an equiaxed layer exists in the bottom region with the maximal f_e reaching 0.32; the equiaxed packing limit ($0.637 \times f_{si}$). With the continuation of solidification, the equiaxed region's thickness increases to approximately 23 mm at the end of solidification, and the maximal f_e reaches 0.8. Figure 8(b) shows the influence of γ on f_e distribution along the vertical line A-A'. The thickness of the equiaxed zone increases with γ .

4.2. Grid sensitivity study

Calculations with four mesh sizes (0.8, 1.0, 1.5 and 2.0 mm) were performed. Figure 9 shows the phase distribution and macrosegregation at the end of solidification. A CET line at about a one-third height from the bottom separates the columnar and equiaxed regions (figure 9(a.x)). It does not seem possible to possess a grid-independent shape of the equiaxed zone but the areas of equiaxed zone for all cases are similar. Macrosegregation distributions of the four cases are shown in figure 9(b.x). According to the figure, the decrease of the grid size from 2.0 to 0.8 mm causes the macrosegregation distribution and segregation intensity to become closer. The case with grid size of 2.0 mm is quite different from other cases. Macrosegregation index range c^{index} and GMI are also labeled in this figure. The c^{index} value for all cases ranges from -32 to 85 . The range does not significantly change when the mesh size decreases more than $\Delta x = 1.5$ mm.

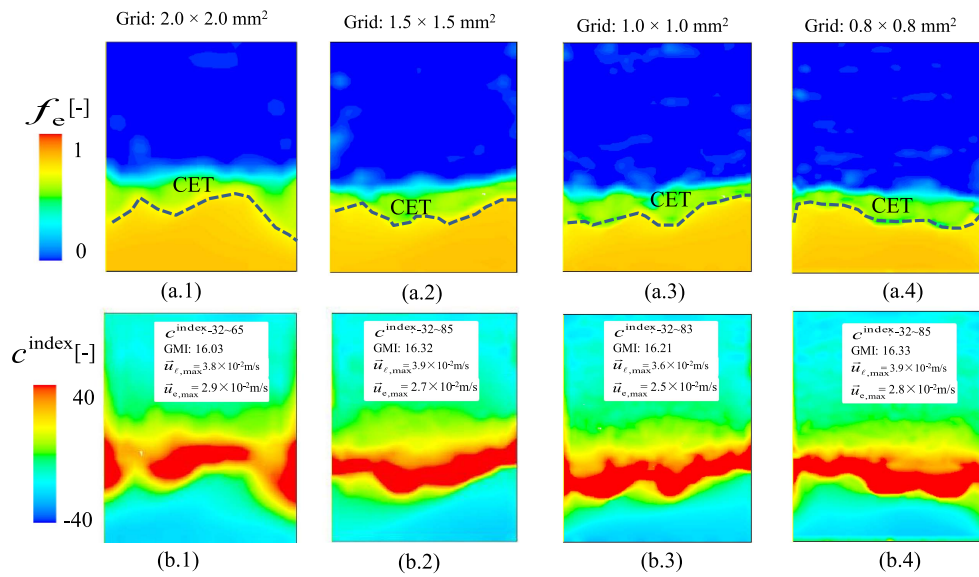


Figure 9. Influence of mesh size on the as-cast structure and macrosegregation. (a.x) Distribution of equiaxed phase (the blue region above the CET line is dominated by the columnar phase); (b.x) macrosegregation contour (c^{index}).

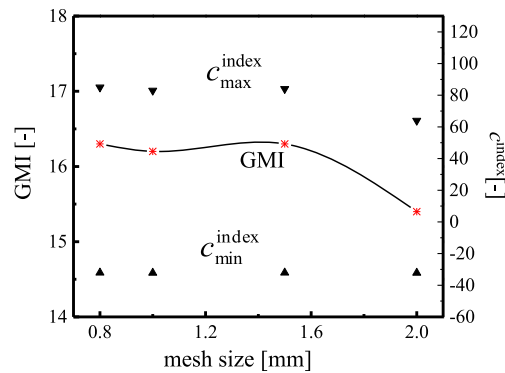


Figure 10. Influence of mesh size on the macrosegregation range and GMI.

Although the macrosegregation patterns for the cases with mesh size smaller than 1.5 mm look rather similar, they cannot converge to a grid-independent result. The macrosegregation is relatively sensitive to the melt convection and crystal sedimentation during the solidification. However, the melt convection greatly interacts with the movement of equiaxed crystals, which are randomly produced through fragmentation. In addition, the velocities of both liquid melt and solid crystals are very sensitive to mesh size. However, the GMI, which can reflect the overall macrosegregation intensity in the domain, can obtain a relatively convergent result (figure 10) when the mesh size is below 1.5 mm.

5. Conclusions

In this study, a fragmentation formulation was proposed and implemented in a volume average model for the mixed columnar-equiaxed solidification. A test case with Sn-10 wt%Pb melt solidifying downward in a 2D domain ($50 \times 60 \text{ mm}^2$) was simulated by assuming that fragmentation is the only source of equiaxed crystals. A reasonable solidification sequence was calculated. The interdendritic flow in the columnar tip growth direction led to the local increase of c_l , promoting remelting and fragmentation. Fragments were produced in the mushy zone near the columnar tip front. These fragments were transported out of the columnar region and continued to grow and sink, and finally settled down and piled up in the bottom domain. The columnar structure, growing from the top, and the pile-up of equiaxed crystals from the bottom finally led to a mixed columnar-equiaxed structure and the occurrence of a CET. A special macrosegregation pattern was predicted, according to which negative segregation occurred in both columnar and equiaxed regions, and a relatively strong positive segregation occurred near the CET line.

The current formulation for the fragmentation considered that transport of a solute-enriched melt through interdendritic flow in the columnar growth direction is in favor of the solute-driven remelting, and hence in favor of fragmentation. One modeling parameter was introduced: the fragmentation coefficient γ . For the fragmentation, the unknown contributing factors, such as the curvature effect of the dendrites, latent heat-induced thermal fluctuation, and diffusion in the interdendritic melt, were included in the single coefficient γ . This coefficient must be determined experimentally or require another theoretical model. The numerical parameter study showed that the influence of γ on the intensity of the flow and equiaxed motion is not significant, and hence its influence on segregation intensity is not significant. The major influence of γ is on the as-cast structure distribution, that is, the larger the γ , the larger the equiaxed zone.

A general issue for the calculation of the multiphase transport phenomena during solidification is the grid size sensitivity. The parameter study showed that the global as-cast structure, that is, the area of equiaxed zone, and the macrosegregation pattern and intensity become insensitive to the grid size when it is smaller than 1.5 mm. Fine details of the structural and compositional distributions are not quantitatively solvable with the current grid resolution.

Acknowledgments

The authors acknowledge the financial support from Austrian Research Promotion Agency (FFG) through the project of Bridge Early Stage (No. 842441), as well as the technical support of the industrial partner Primetals (former Siemens VAI).

ORCID iDs

M Wu  <https://orcid.org/0000-0003-0321-412X>

References

- [1] Beckermann C and Viskanta R 1993 Mathematical modeling of transport phenomena during alloy solidification *Appl. Mech. Rev.* **46** 1–27
- [2] Wu M, Li J, Ludwig A and Kharicha A 2013 Modeling diffusion-governed solidification of ternary alloys: I. Coupling solidification kinetics with thermodynamics *Comput. Mater. Sci.* **79** 830–40

- [3] Wu M, Li J, Ludwig A and Kharicha A 2014 Modeling diffusion-governed solidification of ternary alloys: II. Macroscopic transport phenomena and macrosegregation *Comput. Mater. Sci.* **92** 267–85
- [4] Combeau H, Založnik M, Hans S and Richy P E 2009 Prediction of macrosegregation in steel ingots: influence of the motion and the morphology of equiaxed grains *Metall. Mater. Trans. B* **40** 289–304
- [5] Rappaz M 1989 Modelling of microstructure formation in solidification processes *Int. Mater. Rev.* **34** 93–124
- [6] Wu M and Ludwig A 2006 A three-phase model for mixed columnar-equiaxed solidification *Metall. Mater. Trans. A* **37** 1613–31
- [7] Hellawell A, Liu S and Lu S 1997 Dendrite fragmentation and the effects of fluid flow in castings *JOM* **49** 18–20
- [8] Su Z J, Chen J, Nakajima K and He J C 2009 Criterion for dendrite fragmentation of carbon steel under imposition of linear travelling EMS *Steel Res. Int.* **80** 824–33
- [9] Yasuda H, Yamamoto Y, Nakatsuka N, Nagira T, Yoshiya M, Sugiyama A, Ohnaka I, Umetani K and Uesugi K 2008 *In situ* observation of nucleation, fragmentation and microstructure evolution in Sn–Bi and Al–Cu alloys *Int. J. Cast Met. Res.* **21** 125–8
- [10] Lesoult G 2005 Macrosegregation in steel strands and ingots: characterisation, formation and consequences *Mater. Sci. Eng. A* **413–414** 19–29
- [11] Chalmers B and Williamson R 1965 Crystal multiplication without nucleation *Science* **148** 1717–8
- [12] Garabedian H and Strickland-Constable R 1974 Collision breeding of ice crystals *J. Cryst. Growth* **22** 188–92
- [13] Pilling J and Hellawell A 1996 Mechanical deformation of dendrites by fluid flow *Metall. Mater. Trans. A* **27** 229–32
- [14] Mullis A M, Walker D J, Battersby S E and Cochrane R F 2001 Deformation of dendrites by fluid flow during rapid solidification *Mater. Sci. Eng. A* **304** 245–9
- [15] Jackson K, Hunt J, Uhlmann D and Seward T 1966 On origin of equiaxed zone in castings *Trans. Metall. Soc. AIME* **236** 149–58
- [16] Christenson M and Incropera F 1989 Solidification of an aqueous ammonium chloride solution in a rectangular cavity: I. Experimental study *Int. J. Heat Mass Transfer* **32** 47–68
- [17] Christenson M, Bennon W and Incropera F 1989 Solidification of an aqueous ammonium chloride solution in a rectangular cavity: II. Comparison of predicted and measured results *Int. J. Heat Mass Transfer* **32** 69–79
- [18] Montgomery W and Incropera F 1998 Fragmentation of dendritic crystals during solidification of aqueous ammonium chloride *Exp. Heat Transfer* **11** 59–86
- [19] Paradies C, Smith R and Glicksman M 1997 The influence of convection during solidification on fragmentation of the mushy zone of a model alloy *Metall. Mater. Trans. A* **28** 875–83
- [20] Mathiesen R, Arnberg L, Bleuet P and Somogyi A 2006 Crystal fragmentation and columnar-to-equiaxed transitions in Al–Cu studied by synchrotron x-ray video microscopy *Metall. Mater. Trans. A* **37** 2515–24
- [21] Jung H, Mangelinck-Noel N, Nguyen-Thi H, Bergeon N, Billia B, Buffet A, Reinhart G, Schenk T and Baruchel J 2009 Fragmentation in an Al–7 wt% Si alloy studied in real time by x-ray synchrotron techniques *Int. J. Cast Met. Res.* **22** 208–11
- [22] Liotti E, Lui A, Vincent R, Kumar S, Guo Z, Connolley T, Dolbnya I, Hart M, Arnberg L and Mathiesen R 2014 A synchrotron x-ray radiography study of dendrite fragmentation induced by a pulsed electromagnetic field in an Al–15Cu alloy *Acta Mater.* **70** 228–39
- [23] Leriche N, Combeau H, Gandin C-A and Založnik M 2015 *IOP Conf. Ser.: Mater. Sci. Eng.* **84** 012087
- [24] Flemings M C and Nereo G E 1967 Macrosegregation: I *Trans. Metall. Soc. AIME* **239** 1449–62
- [25] Campanella T, Charbon C and Rappaz M 2004 Grain refinement induced by electromagnetic stirring: a dendrite fragmentation criterion *Metall. Mater. Trans. A* **35** 3201–10
- [26] Wu M and Ludwig A 2007 Using a three-phase deterministic model for the columnar-to-equiaxed transition *Metall. Mater. Trans. A* **38** 1465–75
- [27] Beckermann C 1997 Modeling segregation and grain structure development in equiaxed solidification with convection *JOM* **49** 13–7
- [28] Wu M and Ludwig A 2009 Modeling equiaxed solidification with melt convection and grain sedimentation: II. Model verification *Acta Mater.* **57** 5632–44

- [29] Wu M and Ludwig A 2009 Modeling equiaxed solidification with melt convection and grain sedimentation: I. Model description *Acta Mater.* **57** 5621–31
- [30] Wu M, Ludwig A and Kharicha A 2017 A four phase model for the macrosegregation and shrinkage cavity during solidification of steel ingot *Appl. Math. Modelling* **41** 102–20
- [31] Zheng Y, Wu M, Kharicha A and Ludwig A 2016 Numerical analysis of macrosegregation in vertically solidified Pb–Sn test castings: II. Equiaxed solidification *Comput. Mater. Sci.* **124** 456–70
- [32] Wu M, Zheng Y, Kharicha A and Ludwig A 2016 Numerical analysis of macrosegregation in vertically solidified Pb–Sn test castings: I. Columnar solidification *Comput. Mater. Sci.* **124** 444–55
- [33] Bellet M, Combeau H, Fautrelle Y, Gobin D, Rady M, Arquis E, Budenkova O, Dussoubs B, Duterrail Y and Kumar A 2009 Call for contributions to a numerical benchmark problem for 2D columnar solidification of binary alloys *Int. J. Therm. Sci.* **48** 2013–6
- [34] Ahmad N, Rappaz J, Desbiolles J-L, Jalanti T, Rappaz M, Combeau H, Lesoult G and Stomp C 1998 Numerical simulation of macrosegregation: a comparison between finite volume method and finite element method predictions and a confrontation with experiments *Metall. Mater. Trans. A* **29** 617–30
- [35] Klassen M and Cahoon J 2000 Interdiffusion of Sn and Pb in liquid Pb–Sn alloys *Metall. Mater. Trans. A* **31** 1343–52
- [36] Rocha O L, Siqueira C A and Garcia A 2003 Heat flow parameters affecting dendrite spacings during unsteady-state solidification of Sn–Pb and Al–Cu alloys *Metall. Mater. Trans. A* **34** 995–1006
- [37] Cadirli E and Gündüz M 2000 The directional solidification of Pb–Sn alloys *J. Mater. Sci.* **35** 3837–48